

# Quantum site percolation on triangular lattice and the integer quantum Hall effect

V. V. Mkhitaryan and M. E. Raikh

Department of Physics, University of Utah, Salt Lake City, UT 84112

Generic *classical* electron motion in a strong perpendicular magnetic field and random potential reduces to the *bond* percolation on a *square* lattice. Here we point out that for certain smooth 2D potentials with  $120^\circ$  rotational symmetry this problem reduces to the *site* percolation on a *triangular* lattice. We use this observation to develop an approximate analytical description of the integer quantum Hall transition. For this purpose we devise a quantum generalization of the real-space renormalization group (RG) treatment of the site percolation on the triangular lattice. In quantum case, the RG transformation describes the evolution of the *distribution* of the  $3 \times 3$  scattering matrix at the sites. We find the fixed point of this distribution and use it to determine the critical exponent,  $\nu$ , for which we find the value  $\nu \approx 2.3 \div 2.76$ . The RG step involves only a *single* Hikami box, and thus can serve as a minimal RG description of the quantum Hall transition.

PACS numbers: 72.15.Rn, 73.20.Fz, 73.43.-f

## I. INTRODUCTION

A seminal Chalker-Coddington model Ref. 1 of the integer quantum Hall transition can be introduced in a natural way with the help of a two-dimensional potential

$$U(x, y) = \cos(\pi x) \cos(\pi y). \quad (1)$$

In this potential, the equipotential lines  $U(x, y) = 0$  form a square lattice. For any nonzero  $\varepsilon$ , equipotentials  $U(x, y) = \varepsilon$  are closed. For positive  $\varepsilon$  these equipotentials encircle the maxima  $(x, y) = (2m, 2n)$  [and also  $(2m + 1, 2n + 1)$ ] of  $U(x, y)$ , while for  $\varepsilon < 0$  equipotentials encircle the minima  $(x, y) = (2m, 2n + 1)$  [and  $(2m + 1, 2n)$ ] of  $U(x, y)$ . In a strong perpendicular magnetic field 2D electron drifts along equipotentials. Then reconfiguration of equipotentials at  $\varepsilon = 0$ , as illustrated in Fig. 1a, manifests the change in the character of motion.

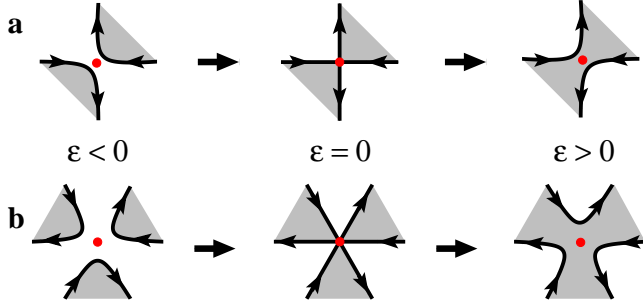


FIG. 1: (Color online) (a) Evolution of equipotentials near the saddle point of potential Eq. (1) as the energy  $\varepsilon$  crosses over from  $\varepsilon < 0$  to  $\varepsilon > 0$ ; (b) evolution of equipotentials near the nodes of potential Eq. (4) with  $\varepsilon$ . Three equipotential lines touch at  $\varepsilon = 0$ .

Chalker and Coddington<sup>1</sup> captured the quantum character of motion in  $U(x, y)$  by assigning to the saddle points at  $(x_m, y_n) = (m - \frac{1}{2}, n - \frac{1}{2})$  where it behaves as

$$U(x - x_m, y - y_n) \approx \quad (2)$$

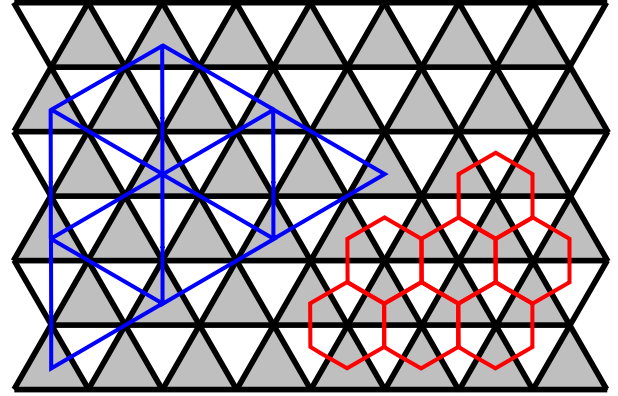


FIG. 2: (Color online) Equipotential lines  $\varepsilon = 0$  of the potential Eq. (4) constitute a triangular lattice. Minima of  $W(x, y)$  are in the centers of shaded triangles. Blue lines constitute a triangular lattice of supersites with lattice constant,  $\sqrt{3}$ . Red lines: hexagonal lattice with sites in the centers of triangles. Each site of a triangular lattice is surrounded by a hexagon.

$$(-1)^{m+n} \pi^2 (x - x_m)(y - y_n) = (-1)^{m+n} \frac{\pi^2 \rho^2}{2} \sin 2\varphi,$$

a scattering matrix

$$S_{cc}(\varepsilon) = \begin{pmatrix} \frac{1}{\sqrt{2}} + \varepsilon & \frac{1}{\sqrt{2}} - \varepsilon \\ -\frac{1}{\sqrt{2}} + \varepsilon & \frac{1}{\sqrt{2}} + \varepsilon \end{pmatrix}. \quad (3)$$

Here  $\rho$  and  $\varphi$  are the polar coordinates with origin at  $(x_m, y_n)$ . Since the magnitude of  $U(x, y)$  is set to be 1, the dimensionless energy,  $\varepsilon$ , is measured in the units of the saddle-point energy width,  $\Gamma = l^2$ , where  $l \ll 1$  is the ratio of magnetic length to the period of potential. Chalker and Coddington demonstrated that, in order to account for a smooth disorder it is sufficient to assume that the phases, acquired by a drifting electron between the saddle points, are random.

In this paper we show that the description of the quan-

tum Hall transition can be obtained basing on a potential

$$W(x, y) = \sum_{n,m} V(\mathbf{r} - n\mathbf{e}_1 - m\mathbf{e}_2), \quad (4)$$

which has a *triangular* symmetry, i.e.,  $\mathbf{e}_1 = (1, 0)$  and  $\mathbf{e}_2 = (1/2, \sqrt{3}/2)$  are the basis unit vectors of a triangular lattice; the function  $V$  is defined inside a “black half” of the rhombus-shape unit cell, see Fig. 2, in the following way

$$V(\rho, \varphi) = \left[ \rho \cos\left(\varphi - \frac{\pi}{6}\right) - \frac{1}{2\sqrt{3}} \right] \times \left[ \rho \cos\left(\varphi - \frac{5\pi}{6}\right) - \frac{1}{2\sqrt{3}} \right] \left[ \rho \cos\left(\varphi - \frac{3\pi}{2}\right) - \frac{1}{2\sqrt{3}} \right]. \quad (5)$$

Here  $\rho$  and  $\varphi$  are the polar coordinates with respect to the origin at  $(\mathbf{e}_1 + \mathbf{e}_2)/3$ . The form of potential in the “white half” of a unit cell is given by Eq. (4) upon replacement  $V(\rho, \varphi) \rightarrow -V(\rho, \varphi - \pi/3)$  and shifting the origin to the center of the white triangle.

Equipotentials of Eq. (5) evolve, as  $\varepsilon$  passes through 0, in a fashion qualitatively different from the case of quadratic symmetry. As shown in Fig. 1a, in the case of quadratic symmetry, black regions (minima) get connected, while adjacent white regions (maxima) get disconnected. By contrast, the behavior of the potential  $W(x, y)$  near the nodes at  $\mathbf{r}_{m,n} = (m - 1/3)\mathbf{e}_1 + (n - 1/3)\mathbf{e}_2$  is given by

$$W(\rho, \varphi) = -\rho^2 \sum_{q=0}^{\infty} c_q \sin[3(2q+1)\varphi], \quad (6)$$

where  $c_q = \frac{2\sqrt{3}}{\pi} [(2q+1)(9(2q+1)^2 - 4)]^{-1}$ . Corresponding evolution of equipotentials is illustrated in Fig. 1b. We see that, as  $\varepsilon$  crosses zero, *three* black regions get joined at  $\varepsilon = 0$  *simultaneously*. This suggests that quantum mechanical description of motion in the potential  $W(x, y)$  requires, in addition to random phases on the links, introducing a  $3 \times 3$  scattering matrix at each node. Below we argue that the form of this matrix is

$$S_{\Delta}(\varepsilon) = \begin{pmatrix} \frac{2}{3}(1+\varepsilon) & -\frac{1}{3} & \frac{2}{3}(1-\varepsilon) \\ \frac{2}{3}(1-\varepsilon) & \frac{2}{3}(1+\varepsilon) & -\frac{1}{3} \\ -\frac{1}{3} & \frac{2}{3}(1-\varepsilon) & \frac{2}{3}(1+\varepsilon) \end{pmatrix}. \quad (7)$$

With matrices Eq. (7) in the nodes, the corresponding network model is shown in Fig. 3. It can be treated numerically using the same MacKinnon-Kramer finite-size scaling algorithm<sup>2</sup> that was employed in Ref. 1 (for subsequent numerical studies of the Chalker-Coddington model see Refs. 3,4,5,6,7,8,9,10,11,12,13,14,15 and review articles<sup>16</sup>).

The advantage of the network Fig. 3 is that its renormalization group (RG) analysis carried out below is easier than the RG analysis<sup>17,18,19,20,21</sup> of the Chalker-Coddington model. This analysis is presented in Sections II-V.

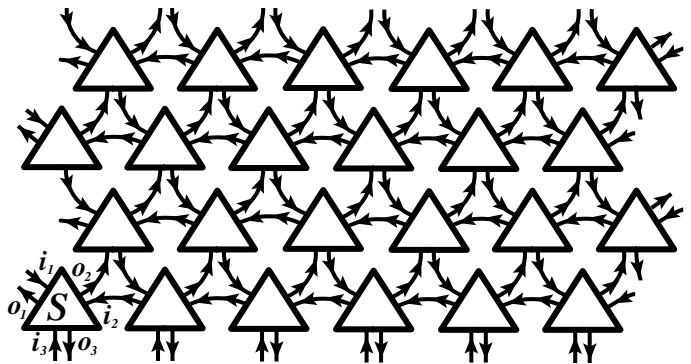


FIG. 3: (Color online) Network model on a triangular lattice is illustrated. Three links enter a node and three links exit each node; the nodes with  $S$ -matrices Eq. (7) are depicted as triangles.

## II. RG PROCEDURE FOR CLASSICAL PERCOLATION ON A TRIANGULAR NETWORK

As in Chalker-Coddington model, in the network Fig. 3 the phases on the links are random, while all  $S$ -matrices in the nodes Eq. (7) are the same. However, in order to develop the RG description, it is necessary to incorporate disorder into the  $S$ -matrices. The reason is that at each RG-step *three*  $S$ -matrices, connected by the links, are combined into one *super- $S$* -matrix. Then the randomness in phases translates into the randomness of the elements of *super- $S$* -matrix.

A natural way to devise the quantum RG description is to start from a classical problem of electron drift along the sides of triangles, Fig. 2.

### A. Classical drift on triangular lattice

Assume that the potential  $W(x, y)$  is perturbed near the nodes, as

$$W(\rho, \phi) = V_0 - c_0\rho^2 \sin(3\varphi) - c_1\rho^2 \sin(9\varphi) - \dots, \quad (8)$$

where the random shift,  $V_0$ , is much smaller than 1, but much bigger than the “quantum” energy width,  $\Gamma$ . Depending on the shift, an electron drifting along equipotential  $W = \varepsilon$  towards a node turns either to the left ( $V_0 < \varepsilon$ ) or to the right ( $V_0 > \varepsilon$ ), see Fig. 1b. We can conventionally call the nodes with  $V_0 < \varepsilon$  and  $V_0 > \varepsilon$  as “black” and “white” lattice sites, respectively. It is obvious that when the average,  $\langle V_0 \rangle$ , is zero, the percolation threshold in the potential Eq. (8) is  $\varepsilon = 0$ . In the language of sites, the same is to say that at  $\varepsilon = 0$  50% of sites are black. It is in fact well-known that the exact threshold for site percolation on a triangular lattice is 50%. However, it is much less obvious that there is a *complete equivalence* between electron drift in potential Eq. (8) and the site percolation on a triangular lattice.

Superficially, this can be seen from the fact that when two neighboring sites are black, they are connected via the black region. Still a rigorous proof requires additional steps, in particular, introducing auxiliary hexagons, see Fig. 2. This proof is given in the Appendix A.

### B. Classical RG scheme

The above mapping on the percolation problem allows one to employ the RG approach to the site percolation on triangular lattice put forward in Ref. 22. This procedure is much simpler than the RG for the bond percolation on the square lattice, proposed in the same paper. Note in passing that the bond percolation on the square lattice is the classical limit of the Chalker-Coddington model<sup>17</sup>.

As shown in Fig. 2, at each RG step<sup>22</sup> the lattice constant increases by a factor of  $\sqrt{3}$ . A site of a new lattice, a *supersite*, is either black or white depending on the colors of the three constituting sites: if either *all three* or *only two* out of three constituting sites are black, then the supersite is black. Otherwise, the supersite is white. Quantitatively, the probability  $p'$  for a supersite to be black is expressed via the corresponding probability for the original site as

$$p' = R(p) = p^3 + 3p^2(1-p). \quad (9)$$

Fixed point,  $p' = p = p_c$ , of the transformation Eq. (9) reproduces the exact result  $p_c = 1/2$ . Critical exponent is determined by the condition that the correlation radius,  $\xi = (p - p_c)^{-\nu}$ , on the original lattice is equal to the correlation radius  $\sqrt{3}(p' - p_c)^{-\nu}$  on the renormalized lattice, i.e.

$$\nu = \frac{\ln(\sqrt{3})}{\ln\left(\frac{dp'}{dp}\right)_{p=p_c}} = \frac{\ln(\sqrt{3})}{\ln(3/2)}. \quad (10)$$

Eq. (10) yields  $\nu = 1.354$ , which differs from the exact value,  $\nu = 4/3$ , by only 1.6%.

The rationale behind the transformation Eq. (9) is that the supersite is located in the center of the black cell in Fig. 2. Then the color of the supersite reflects the “percolation ability” of this black triangular cell, so that, even if one of the nodes, constituting the vertices of the triangular cell is white, the cell still percolates “over black”.

### C. RG in the language of potential shifts

At this point we make an observation that the above RG procedure can be reformulated in the language of potential  $W(x, y)$  with random shifts in the nodes,  $V_0$ . Namely, for  $V_0^1, V_0^2$ , and  $V_0^3$  being the shifts at the nodes constituting a supernode, the shift  $V_0'$  of the supernode is defined as

$$V_0' = \text{Mid}\{V_0^1, V_0^2, V_0^3\}, \quad (11)$$

where Mid stands for  $V_0$  which is *smaller than maximal* but *larger than minimal* out of the three numbers. With  $V_0'$  defined by Eq. (11), the RG equation Eq. (9) describes the evolution of probability that the shift exceeds  $\varepsilon$ .

The importance of the above observation is that reformulation of classical RG procedure in terms of potential shifts opens a possibility to capture the quantum-mechanical motion in the random potential. A prescription how to extend classical description to the quantum case is<sup>17</sup>: the algorithm Eq. (11) should be cast in the form of a *scattering problem*.

### III. REFORMULATION IN TERMS OF CLASSICAL TRANSMISSION

We identify the scattering object as a point where three equipotentials come close as shown in Fig. 4. Incident electron,  $i_1$ , either proceeds along the same equipotential into  $o_1$  (reflection) or switches equipotentials and proceeds along  $o_2$ . Retention of equipotential (reflection) corresponds to positive  $V_0 - \varepsilon$  in the vertex. In terms of scattering matrix

$$\begin{pmatrix} o_1 \\ o_2 \\ o_3 \end{pmatrix} = S \begin{pmatrix} i_1 \\ i_2 \\ i_3 \end{pmatrix}, \quad (12)$$

the same simple notion can be reformulated as follows. For positive  $V_0 - \varepsilon$ , the matrix  $S = S_+$  is a *unit matrix*, while for negative  $V_0 - \varepsilon$  the matrix  $S = S_-$  has the form

$$S_- = \begin{pmatrix} 0 & 0 & 1 \\ 1 & 0 & 0 \\ 0 & 1 & 0 \end{pmatrix}.$$

Superscattering object consists of three scattering objects, and is shown in the same figure.

Now we reformulate Eqs. (9) and (11) in yet another language of  $S$ -matrices. Namely, the  $S$ -matrix of a superscattering object is expressed via  $S$ -matrices of constituting scattering objects upon reducing the number of legs from 12 to 6. We emphasize that this reduction can be carried out in two distinct ways, as illustrated in Fig. 5. The first way is to perform contractions as  $o_2 \leftrightarrow i_2$ ,  $o_4 \leftrightarrow i_4$ , and  $o_6 \leftrightarrow i_6$ . The second variant of contractions is  $o_2 \leftrightarrow i_1$ ,  $o_4 \leftrightarrow i_3$ , and  $o_6 \leftrightarrow i_5$ . Now it is straightforward to check that RG transformation Eq. (11) corresponds to the following rule for  $S$ -matrix of the superscattering object,  $\tilde{S}$ . If the  $S$ -matrices of either all three or only two of constituting objects are  $S_+$ , then  $\tilde{S} = S_+$ . In all other realizations, when at least two of constituting objects have the matrix  $S_-$ , we have  $\tilde{S} = S_-$ . It is important to note that the above rule for  $\tilde{S}$  applies *independently* of the way in which the contractions in Fig. 5 are performed. This is not the case in the quantum version to which we now turn.

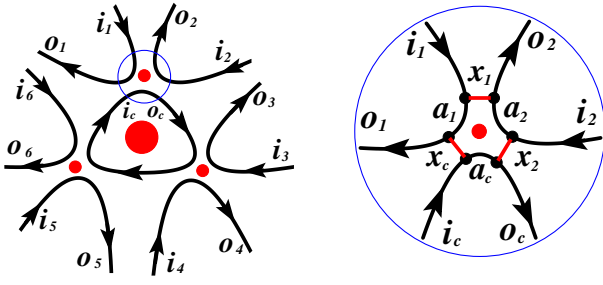


FIG. 4: (Color online) Left: superscattering object is shown with a big red dot, while constituting scattering objects are shown with small red dots. Right: detailed structure of the scattering object; black dots show the points of the close contact of equipotentials. Electron incident along equipotential,  $i$ , can either proceed along the same equipotential,  $a$ , or switch equipotential with probability  $|x|^2$ . The latter processes are illustrated with red dashes.

#### IV. QUANTUM GENERALIZATION

Quantum  $S$ -matrix of the scattering object differs from  $S_+$  and  $S_-$  in two respects. Firstly, at the points of close contact between each pair of equipotentials electron can switch equipotential *even for positive*  $V_0 - \varepsilon$ , when it is forbidden classically. Corresponding classically forbidden transitions are illustrated in Fig. 4 with red dashes. Secondly, upon travelling between two subsequent points of close contact, electron accumulates the Aharonov-Bohm phase,  $\phi_i$ . For example, the phase  $\phi_1$  is accumulated in course of drift between  $i_1$  and  $o_1$ . These phases are irrelevant in the classical limit when the reflection amplitudes,  $y_i$ , are either 0 or 1. However, for intermediate  $0 < y_i < 1$  the amplitude for an electron to execute a close contour around the center in Fig. 4 following the red dashes in the clockwise direction is *finite*. As a result,  $\phi_i$ , enter into quantum scattering matrix. Explicit form of  $S$  in terms of  $0 < y_i < 1$  and  $\phi_i$  can be obtained by solving three pairs of linear equations, describing quantum scattering at each of three points of the close contact of equipotentials. We have

$$S = \frac{-1}{1 - x_1 x_2 x_3 e^{i\psi}} \times \begin{pmatrix} y_1 y_3 e^{i\phi_1} & x_1 y_2 y_3 e^{i(\phi_1 + \phi_2)} & x_1 x_2 e^{i\psi} - x_3 \\ x_2 x_3 e^{i\psi} - x_1 & y_1 y_2 e^{i\phi_2} & y_1 x_2 y_3 e^{i(\phi_2 + \phi_3)} \\ y_1 y_2 x_3 e^{i(\phi_1 + \phi_3)} & x_1 x_3 e^{i\psi} - x_2 & y_2 y_3 e^{i\phi_3} \end{pmatrix}, \quad (13)$$

where  $x_j = \sqrt{1 - y_j^2}$  stand for the transmission amplitudes, and

$$\psi = \phi_1 + \phi_2 + \phi_3 \quad (14)$$

is the net phase accumulated along the closed contour. It is easy to check that the matrix Eq. (13) is unitary. It is also straightforward to verify that in the classical limits,

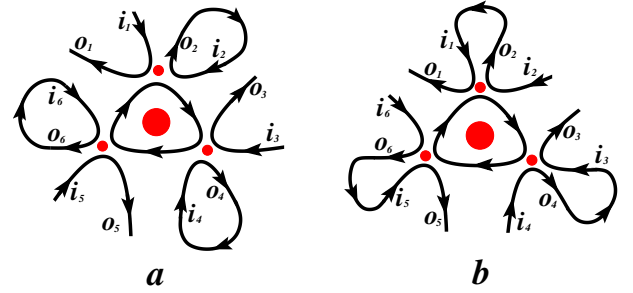


FIG. 5: (Color online) Two contributions to the kernel Eq. (19) originating from two variants of contraction of equipotentials are illustrated; (a) corresponds to  $\tilde{x}^a$ , Eq. (16), while (b) corresponds to  $\tilde{x}^b$ , Eq. (17).

when *all*  $x_j = 0$  or  $x_j = 1$ , Eq. (13) correctly reproduces  $S_+$  and  $S_-$ , respectively.

#### A. The form of the matrix $S_\Delta$

From Eq. (13) we can establish the form of the scattering matrix  $S_\Delta(\varepsilon)$ , Eq. (7), with the help of the following duality argument. Due to triangular symmetry of the potential  $\rho^2 \sin(3\varphi)$  we have  $x_1 = x_2 = x_3 = x$ . Consider now the transition point,  $\varepsilon = 0$ . At this point the probability for electron incident along, say,  $i_1$  (see Fig. 4) to be deflected along  $o_1$  to the left is equal to the probability to be deflected along  $o_2$  to the right. Less trivial is that the phase,  $\psi$ , must be zero at  $\varepsilon = 0$ . This is the consequence of the fact that the scattering problem for electron with energy  $\varepsilon$  and  $-\varepsilon$  are equivalent if we change the drift direction from clockwise to anti-clockwise; this change implies also the change in the sign of  $\psi$ . With  $\psi = 0$ , the condition,  $(1 - x^2)^2 = (x^2 - x)^2$ , of “equal deflection” to the left and to the right, yields a single physical root  $x = -1/2$ . Substituting it back in the matrix Eq. (13) reduces it to the scattering matrix Eq. (7) with  $\varepsilon = 0$ . Then for probabilities  $i_1 \rightarrow o_1$  and  $i_1 \rightarrow o_2$  we get  $4/9$ , while the probability  $i_1 \rightarrow o_3$  is  $1/9$ . Including small finite  $\varepsilon$  can be also performed with the help of the duality argument, namely that the probability of deflection to the left with energy  $\varepsilon$  is equal to the probability of deflection to the right with energy  $-\varepsilon$ . On the other hand, the change of probability  $i_1 \rightarrow o_3$  with  $\varepsilon$  is  $\propto \varepsilon^2$ .

#### B. Quantum RG equation

We now turn to the quantum RG procedure. In contrast to evolution of probability,  $p$ , upon rescaling of the lattice constant in the classical case, this procedure is formulated in terms of evolution of the *distribution function*,  $Q(x)$ , of the *absolute values* of the transmission amplitudes,  $x_i$ . Thus the quantum generalization of Eq. (9)

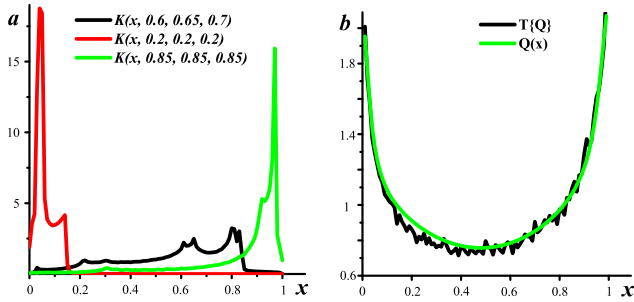


FIG. 6: (Color online) Left: Kernel  $K(x, x_1, x_2, x_3)$  is plotted from Eq. (19) for three sets  $(x_1, x_2, x_3)$ . Right: approximate analytical solution (green line) of the RG equation Eq. (21), given by Eq. (22), is plotted together with r.h.s. of Eq. (21), which is  $\mathbb{T}\{Q(x)\}$  (black line).

at the step  $n$  is the following recurrence relation

$$\begin{aligned} Q_{n+1}(x) &= \mathbb{T}\{Q_n(x)\} \\ &= \int \left( \prod_{j=1}^3 dx_j Q_n(x_j) \right) K(x, x_1, x_2, x_3). \end{aligned} \quad (15)$$

The kernel,  $K$ , represents the conditional probability that, after performing the contractions, the transmission coefficient  $i_c \rightarrow o_1$  in Fig. 4 is equal to  $x$ , provided that the constituting transmission coefficients are  $x_1, x_2$ , and  $x_c = x_3$ , as illustrated in Fig. 4. In analytical evaluation of the dependence  $x(x_1, x_2, x_3)$  it is important to take into account that this dependence is different for two variants of contractions. For a variant  $o_2 \leftrightarrow i_2$ , shown in Fig. 5a, the transmission coefficient is given by

$$\begin{aligned} |\tilde{x}_c^a|^2 &= \\ 1 - \left| \frac{\left( \sqrt{1-x_1^2} e^{i\varphi} + \sqrt{1-x_2^2} \right) \sqrt{1-x_3^2}}{(1-x_1 x_2 x_3 e^{i\psi}) e^{i\varphi} + \sqrt{(1-x_1^2)(1-x_2^2)}} \right|^2, \end{aligned} \quad (16)$$

where  $\varphi$  is the phase along the contour  $(o_2, i_2)$ , which is now *closed*. Correspondingly, for the second kind of closing  $o_2 \leftrightarrow i_1$ , Fig. 5b, the transmission coefficient has the form

$$\begin{aligned} |\tilde{x}_c^b|^2 &= \\ 1 - \left| \frac{(x_1 - e^{i\varphi}) \sqrt{(1-x_2^2)(1-x_3^2)}}{(1-x_1 x_2 x_3 e^{i\psi}) e^{i\varphi} + x_2 x_3 e^{i\psi} - x_1} \right|^2, \end{aligned} \quad (17)$$

where  $\varphi$  stands for the phase along  $(o_2, i_1)$ . For details of derivation of Eqs. (16), (17) see Appendix B.

Relations Eqs. (16), (17) define also the dependencies  $\tilde{x}_1^{a,b}(x_1, x_2, x_3)$  and  $\tilde{x}_2^{a,b}(x_1, x_2, x_3)$ . It is important that the central phase,  $\psi$ , is common for all three dependencies  $\{\tilde{x}_j^a(\{x_i\}, \varphi_j, \psi)\}_{j=1,2,3}$  and  $\{\tilde{x}_j^b(\{x_i\}, \varphi_j, \psi)\}_{j=1,2,3}$ . A crucial step in extending classical RG procedure to

the quantum case is to follow the prescription to choose a *middle* out of three coefficients

$$\begin{aligned} \tilde{x}^a(\{x_i\}, \{\varphi_i\}, \psi) &= \\ \text{Mid} \left( \tilde{x}_1^a(\{x_i\}, \varphi_1, \psi), \tilde{x}_2^a(\{x_i\}, \varphi_2, \psi), \tilde{x}_3^a(\{x_i\}, \varphi_3, \psi) \right), \end{aligned} \quad (18)$$

and the same for  $\tilde{x}^b(\{x_i\}, \{\varphi_i\}, \psi)$ . Eq. (18) is a quantum generalization of the classical Eq. (11). Note that selection of middle value in Eq. (18) is performed for *given* values of random phases,  $\varphi_1, \varphi_2, \varphi_3$ , and  $\psi$ . Within RG procedure different phases are uncorrelated, and in evaluation of the kernel we average over each of four phases independently. Finally, taking into account that contractions  $a$  and  $b$  are statistically equivalent, the expression for  $K(x, \{x_i\})$  acquires the form

$$\begin{aligned} K(x, \{x_i\}) &= \frac{1}{2} \left\langle \delta(x - \tilde{x}^a(\{x_i\}, \{\varphi_i\}, \psi)) \right\rangle_{\{\varphi_i, \psi\}} \\ &+ \frac{1}{2} \left\langle \delta(x - \tilde{x}^b(\{x_i\}, \{\varphi_i\}, \psi)) \right\rangle_{\{\varphi_i, \psi\}}. \end{aligned} \quad (19)$$

Quantum delocalization corresponds to the fixed point of the transformation Eq. (15). It is found in the next Section.

## V. NUMERICAL RESULTS FOR FIXED POINT AND CRITICAL EXPONENT

### A. Kernel

The examples of the kernel,  $K(x)$ , calculated using Mathematica from Eqs. (16)-(19), are plotted in Fig. 6 for different sets  $x_1, x_2, x_3$ . It is seen that the kernel supports the attractive critical points  $x_1 = x_2 = x_3 = 0$  and  $x_1 = x_2 = x_3 = 1$ . Indeed, for values  $x_1 = x_2 = x_3 = 0.2$ , the kernel is centered at even smaller value  $x \approx 0.04$ , while for  $x_1 = x_2 = x_3 = 0.85$  it is around bigger value  $x \approx 0.95$ . In both cases the kernel is narrow. This is because for “classical” transmission coefficients interference does not play a role, so that the phases drop out from Eqs. (16), (17). However, for intermediate values  $x_1 = 0.6, x_2 = 0.65, x_3 = 0.7$  the kernel extends over entire interval  $0 < x < 1$ . It also exhibits peaks at  $x = 0.03, 0.61, 0.65, 0.8$  and  $0.83$ . The origin of these peaks is the anomalous contributions of phases at  $\varphi_0 = 0, \pi$  and  $\psi_0 = 0, \pi$  to the kernel. Indeed, for these values of phases we have  $\partial \tilde{x}^{a,b} / \partial \varphi = \partial \tilde{x}^{a,b} / \partial \psi = 0$ , so that

$$\begin{aligned} \tilde{x}^{a,b}(\varphi, \psi) &= \tilde{x}^{a,b}(\varphi_0, \psi_0) + \frac{\partial^2 \tilde{x}^{a,b}}{2} \Big|_{\varphi_0, \psi_0} (\varphi - \varphi_0)^2 \\ &+ \frac{\partial^2 \tilde{x}^{a,b}}{2} \Big|_{\varphi_0, \psi_0} (\psi - \psi_0)^2 + \frac{\partial^2 \tilde{x}^{a,b}}{\partial \varphi \partial \psi} \Big|_{\varphi_0, \psi_0} (\varphi - \varphi_0)(\psi - \psi_0). \end{aligned} \quad (20)$$

It is easy to check that, when the quadratic form of second derivatives is negatively defined, the corresponding contribution to the kernel is  $\propto \ln|x - \tilde{x}^{a,b}(\varphi_0, \psi_0)|$ .

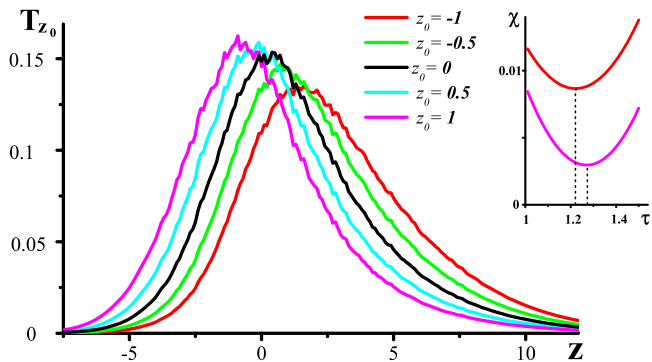


FIG. 7: (Color online)  $T_{z_0} = \mathbb{T}\{\tilde{Q}(z - z_0)\}$  is plotted for different  $z_0$ . Inset shows the variance,  $\chi(\tau)$ , plotted from Eq. (26). The minima correspond to  $\tau = 1.27$  and  $\tau = 1.22$  for  $z_0 = 1$  and  $z_0 = -1$ , respectively.

Therefore the peaks in the kernel reflect the fact that two loops corresponding to phases  $\phi$  and  $\psi$  are insufficient for complete averaging. Still, the phase volume of the singular contributions is small, so that the fixed point of the transformation Eq. (15) is not sensitive to these singularities.

### B. Fixed point

The fixed point,  $Q(x)$ , of the quantum RG equation Eq. (15), satisfies the following nonlinear integral equation

$$Q(x) = \mathbb{T}\{Q(x)\} = \int \left( \prod_{j=1}^3 dx_j Q(x_j) \right) K(x, x_1, x_2, x_3), \quad (21)$$

which we have solved using Mathematica. Starting from initial distribution,  $Q(x) = 1$ , and performing analytical fit at each step of successive approximations the following expression for the fixed point was obtained after the fourth step

$$Q(x) = \frac{0.9}{1 + 10^3 x^2} + \frac{0.9}{1 + 5 \cdot 10^2 (1 - x)^2} + 0.63x^3 + 0.55(1 - x)^3 + 0.6. \quad (22)$$

This expression is plotted in Fig. 6b with a green line. One can judge on the accuracy of the approximate solution Eq. (22) by substituting it into the right-hand side of Eq. (21). The result, black line in Fig. 6b, is indeed very close to Eq. (22).

The fixed point solution rises upon approaching  $x = 0$  and  $x = 1$ . This behavior is inherited from the classical percolation. Note that similar behavior was found in Refs. 17,19 for the fixed point of the quantum bond

percolation on the square lattice. Direct comparison with conductance distribution  $P(G)$  found in Refs. 17,19 can be performed using the relation  $P(G) = Q(\sqrt{G})/2\sqrt{G}$ . This comparison indicates that, while numerically the fixed point distributions are close, Eq. (22) favors small values of  $x$ . Qualitatively, this reflects the fact that at critical energy,  $\varepsilon = 0$ , electron incident along  $i_1$  (see Fig. 4) is more likely to proceed along  $a_1$  rather than switch to  $o_2$ . The asymmetry is seen more clearly if one interprets  $Q(x)$  in terms of distribution,  $\tilde{Q}$  of heights of the effective saddle point. This height is determined by the relation  $x^2 = 1/(e^z + 1)$ , so that

$$\tilde{Q}(z) = \frac{e^z}{2(e^z + 1)^{3/2}} Q([e^z + 1]^{-1/2}). \quad (23)$$

The distribution  $\tilde{Q}(z)$  is shown in Fig. 7 with a black line. It has an asymmetry towards large  $z$ .

### C. Critical exponent

To estimate the critical exponent,  $\nu$ , which governs the divergence of localization radius,  $\xi(\varepsilon) \propto 1/\varepsilon^\nu$ , as a function of energy,  $\varepsilon$ , we used the reasoning from Refs. 17,19. Electron with finite energy,  $\varepsilon \ll \Gamma$ , “sees” the shifted distribution of the saddle point heights  $\tilde{Q}(z - z_0)$ , where  $z_0 \ll 1$  is proportional to  $\varepsilon$ . The key step of the reasoning<sup>17,19</sup> is that, upon the RG transformation, the electron travels on the lattice with the lattice constant  $\sqrt{3}$  and sees the shifted distribution of heights,  $\mathbb{T}\{\tilde{Q}(z - z_0)\} = \tilde{Q}(z - \tau z_0)$ , where  $\tau$  is some constant independent of  $z_0$ . After subsequent  $n$  RG steps this distribution evolves into  $\tilde{Q}(z - \tau^n z_0)$ . When the shift accumulates to reach  $\sim 1$ , the electron becomes localized within the size of a unit cell of renormalized lattice. Then from the relations

$$\xi(z_0) \propto \frac{1}{z_0^\nu}, \quad \xi = (\sqrt{3})^n, \quad z_0 \tau^n \sim 1, \quad (24)$$

we find

$$\nu = \frac{\ln \sqrt{3}}{\ln \tau}. \quad (25)$$

This definition of  $\nu$  is a quantum generalization of Eq. (10). In Fig. 7 the result of calculation  $\mathbb{T}\{\tilde{Q}(z - z_0)\}$  for four  $z_0 = -1, -0.5, 0.5, 1$  is shown. We see that for these  $z_0$  the shape of  $\mathbb{T}\{\tilde{Q}\}$  is only slightly affected by the shift. The curves are approximately equidistant, so that an estimate of  $\tau$  can be obtained simply from the horizontal separation  $\approx 0.4$  between the neighboring curves. This yields  $\tau \approx 1.25$  and, correspondingly,  $\nu \approx 2.46$ . For more accurate estimate we studied the variance,

$$\chi(\tau, z_0) = \sum_{z_i} \left[ \mathbb{T}\{\tilde{Q}(z_i - z_0)\} - \tilde{Q}(z_i - \tau z_0) \right]^2, \quad (26)$$



as a function of  $\tau$  for different values of the “energy shift”  $z_0$ . The sum Eq. (26) was taken over discrete set  $z_i = -10 + 0.01i$  for  $i = 1, 2, \dots, 220$ . In Fig. 7 we plot the variance for  $z_0 = 1$  and  $z_0 = -1$ . Both curves have pronounced minima at  $\tau = 1.27$  and  $1.22$ , respectively. This translates into the values of  $\nu = 2.3$  and  $\nu = 2.76$ . Although these values are in good agreement with known value of  $\nu$ , the accuracy of the above estimate is limited. The limitation is due to the fact that for  $z_0 = \pm 1$  the heights of maxima of the curves  $\text{T}\{\tilde{Q}(z - z_0)\}$ , shown in Fig. 7, differ from the height of  $\tilde{Q}(z)$ . This deviation would not be a problem for smaller  $z_0$ . However for  $z_0 = \pm 0.5$  the variance becomes small, and its dependence on  $\tau$  becomes weak. Apparently, the variance Eq. (26) is affected by the wiggles at the top of the curves  $\text{T}\{\tilde{Q}(z - z_0)\}$  for  $z_0 = \pm 0.5$  stronger than for  $z_0 = \pm 1$ , which makes the evaluation of  $\chi$  for small  $z_0$  ineffective.

## VI. CONCLUSION

It is interesting to point out that, while the classical limit of the Chalker-Coddington model based on potential Eq. (2) reduces to the *bond* percolation, similar form of potential Eq. (8) leads to the *site* percolation. The reason is the symmetry of corresponding potentials. As seen from Fig. 2, the hexagons surrounding the nodes of potential Eq. (8) have common *sides*. On the other hand, the squares, drawn around the nodes of potential Eq. (2) share the *vertices*.

Both the bond percolation on a square lattice and the site percolation on triangular lattice have  $p_c = 1/2$ , which is insured by self-duality. The RG descriptions<sup>22</sup> of both cases, having fixed point,  $p_c = 1/2$ , effectively preserve this self-duality. As a result, the RG values for classical exponent come out close to  $\nu = 4/3$  in both RG schemes. In this paper we demonstrated that quantum extension of classical RG to the triangular lattice also yields the critical exponent close to the known value  $\nu = 2.33$ .

The fact that the simple RG scheme, considered in the present paper, describes the quantum Hall transition so accurately has a deep underlying reason. Delocalized state in the quantum Hall transition emerges as a result of competition of two trends: (i) quantum interference processes that survive in the presence of magnetic field (Hikami boxes, Ref. 23) tend to localize electron, while (ii) classical Lorentz force, by causing electron drift, prevents it from repeating closed diffusive trajectories. Both trends are incorporated into our RG scheme. Obviously, chiral motion is the consequence of the Lorentz force. Hikami boxes, on the other hand, are represented in the RG step in the form of figure-eight trajectories, as illustrated in Fig. 5.

Note finally, that simplicity of the RG description proposed here suggest possibility to extend it to different from quantum Hall universality classes, see, *e.g.*, Refs. 24,25,26,27.

## VII. ACKNOWLEDGEMENTS

We are grateful to I. Gruzberg and V. Kagalovsky for numerous discussions of the network models. This work was supported by the BSF grant No. 2006201.

## APPENDIX A

Here we elaborate on the mapping of the problem of percolation over equipotential lines in the random potential Eq. (8) and the conventional site percolation problem. The easiest way to establish this mapping is to surround all sites of triangular lattice with hexagons, as shown in Fig. 2. If the site is occupied, then the hexagon is, say, black; if the site is vacant, it is white. The distinctive property of the triangular lattice is that, when two hexagons touch, they automatically have a common side. Note in passing, that this is not the case for a square lattice, where two squares, drawn around the sites, may touch by sharing a vertex but not share a side. In the site-percolation problem, the bond between two neighboring sites conducts if both of them are occupied. The same is to say that conduction is possible between two touching hexagons, if they are both black. Percolation threshold corresponds to the portion of black hexagons when conduction over entire sample becomes possible. The fact that  $p_c = 1/2$  is a direct consequence of geometrical arrangement of hexagons, due to which percolation over black hexagons rules out the percolation over white hexagons. Also, due to this arrangement, one of the colors always percolates.

Consider now the potential Eq. (8). Black sites are now those in which  $V_0 < \varepsilon$ . Configuration of equipotentials around this site is the rightmost of three shown in Fig. 1b. Accordingly, configuration of equipotentials around the site with  $V_0 > \varepsilon$  is the leftmost of three shown in Fig. 1b. Consider now two neighboring sites with  $V_0 < \varepsilon$ . Fig. 2 makes it apparent that any two black points inside hexagons surrounding these sites, are connected via black color. Thus, in terms of connectivity over black, two neighboring sites with  $V_0 < \varepsilon$  are completely similar to two neighboring black hexagons. Similarly, as can be seen from Fig. 2, for two neighboring sites with  $V_0 < \varepsilon$  and  $V_0 > \varepsilon$ , the centers of surrounding hexagons are disconnected. The same is true for two neighboring hexagons of opposite colors in the percolation problem. To complete the mapping, we note that, in percolation problem, the connectivity of two neighboring hexagons depends *entirely* on their colors, i.e., it does not depend on the color of the other neighbors. In the same way, in the problem of equipotentials, whether or not two neighboring sites are connected is determined exclusively by the signs of  $V_0 - \varepsilon$  in these sites.

## APPENDIX B

The form of the  $S$ -matrix Eq. (13) can be established with the help of Fig. 4. Matrix  $S$  relates the incident,  $i_1, i_2, i_c$ , and outgoing,  $o_1, o_2, o_c$ , amplitudes via transmission coefficients,  $x_1, x_2$ , and  $x_c$ . The form Eq. (13) follows from the system of six equations, which include also the amplitudes  $a_1, a_2$ , and  $a_c$  between the points of close contact of corresponding equipotentials. As seen from Fig. 4 the amplitudes  $a_1$  and  $a_2$  are related via  $x_1$  as

$$\begin{aligned} a_1 &= x_1 a_2 e^{i\phi_2} + y_1 i_1, \\ o_2 &= -y_1 a_2 e^{i\phi_2} + x_1 i_1. \end{aligned} \quad (\text{B1})$$

The amplitudes  $a_c$  and  $a_1$  are related via  $x_c$

$$\begin{aligned} a_c &= x_c a_1 e^{i\phi_1} + y_c i_c, \\ o_1 &= -y_c a_1 e^{i\phi_1} + x_c i_c. \end{aligned} \quad (\text{B2})$$

Finally, the amplitudes  $a_2$  and  $a_c$  are related via  $x_2$

$$\begin{aligned} a_2 &= x_2 a_c e^{i\phi_c} + y_2 i_2, \\ o_c &= -y_2 a_c e^{i\phi_c} + x_2 i_2. \end{aligned} \quad (\text{B3})$$

In Eqs. (B1)-(B3), the phases  $\phi_1, \phi_2$ , and  $\phi_c$  are the Aharonov-Bohm phases accumulated, respectively, by waves  $a_1, a_2, a_c$  between the points of closed contact. Excluding  $a_1, a_2, a_c$  from Eqs. (B1)-(B3) we recover  $S$ -matrix Eq. (13), in which  $x_3$  stands for  $x_c$  and  $\phi_3$  for  $\phi_c$ .

In order to derive Eq. (16) we set in Eqs. (B1)-(B3)  $i_2 = o_2 e^{i\varphi_2}$ , as enforced by a contraction in Fig. 5a. Upon setting  $i_1 = 0$ , we find the proportionality coefficient between  $o_1$  and  $i_c$ . This recovers Eq. (16), in which  $\varphi = \varphi_2 + \phi_2$ . Similarly, Eq. (17) is recovered upon setting  $i_1 = o_2 e^{i\varphi}$ , as shown in Fig. 5b, and relating the amplitudes  $o_1$  and  $i_c$ .

- 
- <sup>1</sup> J. T. Chalker and P. D. Coddington, *J. Phys. C* **21**, 2665 (1988).  
<sup>2</sup> A. MacKinnon and B. Kramer, *Phys. Rev. Lett.* **47**, 1546 (1981).  
<sup>3</sup> D.-H. Lee, Z. Wang, and S. Kivelson, *Phys. Rev. Lett.* **70**, 4130 (1993).  
<sup>4</sup> D. K. K. Lee and J. T. Chalker, *Phys. Rev. Lett.* **72**, 1510 (1994).  
<sup>5</sup> D. K. K. Lee, J. T. Chalker, and D. Y. K. Ko, *Phys. Rev. B* **50**, 5272 (1994).  
<sup>6</sup> Z. Wang, D.-H. Lee, and X-G. Wen, *Phys. Rev. Lett.* **72**, 2454 (1994).  
<sup>7</sup> I. M. Ruzin and S. Feng, *Phys. Rev. Lett.* **74**, 154 (1995).  
<sup>8</sup> V. Kagalovsky, B. Horovitz, and Y. Avishai, *Phys. Rev. B* **52**, R17044 (1995).  
<sup>9</sup> V. Kagalovsky, B. Horovitz, and Y. Avishai, *Phys. Rev. B* **55**, 7761 (1997).  
<sup>10</sup> Z. Wang, B. Jovanović, and D.-H. Lee, *Phys. Rev. Lett.* **77**, 4426 (1996).  
<sup>11</sup> S. Cho and M. P. A. Fisher, *Phys. Rev. B* **55**, 1637 (1997).  
<sup>12</sup> R. Klesse and M. Metzler, *Phys. Rev. Lett.* **79**, 721 (1997).  
<sup>13</sup> M. Janssen, M. Metzler, and M. R. Zirnbauer, *Phys. Rev. B* **59**, 15836 (1999).  
<sup>14</sup> L. P. Pryadko and A. Auerbach, *Phys. Rev. Lett.* **82**, 1253 (1999).  
<sup>15</sup> R. Klesse and M. R. Zirnbauer, *Phys. Rev. Lett.* **86**, 2094 (2001),  
<sup>16</sup> P. Cain, R. A. Römer, *Adv. Solid State Phys.* **42**, 237 (2003), *Int. J. Mod. Phys. B* **19**, 2085 (2005); E. Shimshoni, *Mod. Phys. Lett. B* **18**, 923 (2004); B. Kramer, T. Ohtsuki, S. Kettemann, *Phys. Rep.* **417**, 211 (2005).  
<sup>17</sup> A. G. Galstyan and M. E. Raikh, *Phys. Rev. B* **56**, 1422 (1997).  
<sup>18</sup> D. P. Arovas, M. Janssen, and B. Shapiro, *Phys. Rev. B* **56**, 4751 (1997).  
<sup>19</sup> P. Cain, R. A. Römer, M. Schreiber, and M. E. Raikh, *Phys. Rev. B* **64**, 235326 (2001).  
<sup>20</sup> P. Cain, R. A. Römer, and M. E. Raikh, *Phys. Rev. B* **67**, 075307 (2003).  
<sup>21</sup> U. Zülicke and E. Shimshoni, *Phys. Rev. B* **63**, 241301(R) (2001).  
<sup>22</sup> P. J. Reynolds, W. Klein, and H. E. Stanley, *J. Phys. C* **10**, L167 (1977).  
<sup>23</sup> S. Hikami, *Phys. Rev. B* **24**, 2671 (1981).  
<sup>24</sup> V. Kagalovsky, B. Horovitz, Y. Avishai, and J. T. Chalker, *Phys. Rev. Lett.* **82**, 3516 (1999).  
<sup>25</sup> T. Senthil, J. B. Marston, and M. P. A. Fisher, *Phys. Rev. B* **60**, 4245 (1999).  
<sup>26</sup> I. A. Gruzberg, A. W. W. Ludwig, and N. Read, *Phys. Rev. Lett.* **82**, 4524 (1999).  
<sup>27</sup> E. J. Beamond, J. Cardy, and J. T. Chalker, *Phys. Rev. B* **65**, 214301 (2002).